



Experimental study on the seismic enhancement of brick masonry spandrels using a single-sided composite reinforced mortar coating

Matija Gams¹ · Ingrid Boem² · Natalino Gattesco² · Emanuele Rizzi² · Allen Dudine³

Received: 27 June 2023 / Accepted: 10 January 2024 / Published online: 12 February 2024
© The Author(s) 2024

Abstract

The paper reports on four cyclic tests of brick masonry spandrels in reference state and strengthened state. The tests were carried out on full-scale, H-shaped masonry panels to investigate the coupling role of the spandrel in connecting two piers in a historical masonry wall subjected to in-plane lateral actions. Two 250-mm-thick solid-brick masonry samples were tested—one single-leaf, the other two-leaves masonry. Both samples were tested before and after strengthening by applying a Composite Reinforced Mortar (CRM) coating on one surface. The CRM coating consisted of a lime mortar coating (nominal thickness = 30 mm), reinforced with mesh made of Glass Fibre-Reinforced Polymer (GFRP) that was anchored to the wall by GFRP transverse connectors. For the double-leaf masonry, there were additional transverse connectors made of steel bars in concrete cores (artificial diatones) to prevent masonry leaves separation and to improve the bonding of the CRM coating to the masonry. The test responses are compared in terms of crack pattern, failure mode, resistance, displacement and energy dissipation capacity. The tests showed the effectiveness of the proposed CRM system, which increased the spandrel resistance by 33% and 125% in the single—and double-leaf masonry, respectively, with the ultimate drift being 3.2% (one order of magnitude greater than for the unstrengthened reference samples). Data on energy dissipation and the equivalent viscous damping are also collected and compared. Importantly, the presence of the reinforcing mesh and the composite action of the coating and the wall changed the damage evolution and response mechanism, which resulted in a much better seismic response.

Keywords Masonry spandrels · Structural strengthening · Single-leaf brick masonry · Double-leaf brick masonry · Textile reinforced mortar · Composite reinforced mortar

✉ Ingrid Boem
ingrid.boem@dia.units.it

¹ Faculty of Civil and Geodetic Engineering, University of Ljubljana, Jamova cesta 2, 1000 Ljubljana, Slovenia

² Department of Engineering and Architecture, University of Trieste, Via Alfonso Valerio 6/1, 34127 Trieste, Italy

³ FibreNet S.p.A., Via Jacopo Stellini, 3 – Z.I.U., 33050 Pavia di Udine, UD, Italy

1 Introduction

The in-plane lateral resistance of masonry piers plays a primary role in the global seismic response of existing masonry buildings. However, masonry spandrels can provide significant coupling, which can influence the load distribution among the piers and their interaction (Tomaževic 1999; Foraboschi 2009; Knox et al. 2017). In this way, they can modify the response mechanism of the structure. For a proper prediction of structural behaviour in masonry buildings, it is thus critical to understand and accurately quantify the resistance and deformation capacities of spandrels. Furthermore, effective strategies to improve their performance should be developed and verified by experimental testing. Knowledge about seismic performance in historical masonry buildings is that much more important because these structures were constructed with only vertical loads in mind. Where spandrels are slender or lack an effective lintel protruding into the piers, their resistance is extremely low and the risk of collapse correspondingly very high. This is typically the case in historical buildings that only have a masonry arch (regular or flat) at the spandrel intrados, as shown by the experimental study performed by Parisi et al. (2014). In their study, the performances of three different tuff masonry spandrel configurations with the same geometries (i.e. a plain masonry arch, a spandrel with a wooden lintel and one with a reinforced-concrete RC ring beam on top) were compared. The worst performances were observed in the first case, due to the high fragility of the arch in opposing to the differential displacements at the supports. Contrastingly, the wooden lintel ensured connection with the piers, avoiding the masonry above from collapsing too early, and the RC ring beam on top prevented separation of the piers until the drift levels were large. Graziotti et al. (2014) evidenced the role of the wooden lintel in increasing the strength of rubble stone spandrels (due to its stiffness) and limiting the number of cracks opening by comparing samples with thick and slender lintels. The presence of horizontal steel ties can furtherly improve the spandrel behaviour, as shown by Graziotti et al. (2012) and Bayer and Dazio (2012). Similarly, the strength and deformation capacities can also be effectively increased by introducing horizontal Fibre Reinforced Polymer (FRP)-bonded laminates (Rinaldin et al. 2017).

A different strengthening technique for spandrels—Composite Reinforced Mortar (CRM)—was investigated in this study. This consists of the application of a mortar coating, reinforced with mesh made of Glass FRP (GFRP), and anchored into the wall by transverse FRP connectors. Since this technique was first developed for piers, CRM has been widely investigated in the literature at both the characterisation test level (Gattesco and Boem 2017a) and in its interaction with the existing masonry in enhancing its in-plane and out-of-plane behaviour (Gattesco and Boem 2015, 2017b). Tests on full-scale masonry piers have also been carried out (Gattesco et al. 2015, 2023a). However, the CRM method is designed for full-surface application and affects the response of the piers as well as the spandrels. The effect of strengthening the spandrels in this way has not yet been directly investigated, the present research being one of the first studies in this field.

Thus, original experimental in-plane cyclic tests were carried out on brick masonry spandrels with and without the CRM reinforcement, which allowed a comparison of the results in terms of strength, deformation capacity and energy dissipation. In particular, solid brick spandrels made of single- and double-leaf solid-brick masonry, without lintels, were investigated. The study focused on the role of the CRM reinforcement applied to only one side of the masonry. Single-sided applications are increasingly attracting the interest of the refurbishment market, because they are faster, cheaper and more practical, allowing continuity of the activities inside the building and the preservation of internal artistic

decorations. However, a reduced reinforcement ratio and the onset of possible out-of-plane parasitic bending due to the eccentric stiffness have to be considered. Also, with multiple-leaf masonry, it is necessary to prevent the leaves separating by introducing elements for effective transverse connection.

Three different approaches can be found in the literature for investigating the coupling effect of masonry spandrels, all of which are based on full-cycle quasi-static cyclic loading.

The first (Parisi et al. 2014; Knox et al. 2017) consists of “TT”-shaped masonry panels, with the two piers fixed at the base, pre-loaded vertically and the lateral cyclic action applied at the height of the spandrel. The results are expressed in the form of global horizontal force varying the horizontal displacement at the top. The test mainly assesses the horizontal capacity of the piers-spandrel assembly, rather than the specific shear performances of the spandrel. In fact, the actual shear force on the spandrel is not known. Also, the piers get often damaged (mostly, cracking at the base), affecting the overall lateral performances. Lastly, the horizontal sliding between the piers is constrained, affecting the spandrel response.

The second approach (Graziotti et al. 2012, 2014; Gattesco et al. 2016) comprises “H”-shaped masonry panels with a central spandrel connecting to lateral piers. The piers are clamped vertically to reproduce carried gravity loads, one pier being fixed at the base, the other moved vertically with increasing amplitude. The test assesses the specific performances of the spandrel, without any damaging occurring in the piers, and the results are presented in terms of shear force varying the vertical displacement between the spandrel’s ends. The horizontal sliding between the piers is free, the piers rotation is constrained.

The third approach (Beyer and Dazio 2012) is again based on “H”-shaped samples, but differs from the second one in the load pattern, with the load being applied by imposed synchronous rotations at the base of the piers. Both the horizontal sliding between the piers and the piers rotation are free. The results are presented in terms of shear force on the spandrel, varying the spandrel distortion evaluated from the piers rotation.

The tests reported on herein were performed according to the latter approach. The main features of the samples and the testing apparatus are reported in the following sections. The test results are then described in terms of capacity curves and damage pattern evolution. Finally, the results are analysed and compared, providing useful information on the effectiveness of the CRM coating in terms of its resistance, displacement, stiffness and dissipative capacities.

2 Sample characteristics

The investigated masonry was built using solid clay bricks ($120 \times 55 \times 250 \text{ mm}^3$, width \times height \times length) assembled using natural lime mortar (with $\sim 10\text{-mm}$ -thick joints). The bricks had a surface roughness reproducing the typical appearance of old masonry structures. The compressive strength of the bricks was determined by testing six single solid units, in accordance to EN 771-1:2011 + A1:2015 (2015): it emerged an average compressive strength of 20.8 MPa (dev. st 4%) and a normalised compressive strength equal to 15.7 MPa. The mortar simulated the weak mortar typically found in historical buildings. This comprised a mixture of natural hydraulic lime and sand, in a mass ratio of about 1:7. The flexural ($f_{b,f}$) and compressive ($f_{b,c}$) strength of the mortar were determined by testing prisms with dimensions of $40 \times 40 \times 160 \text{ mm}^3$. Compression tests on the halves resulting

from the three-point bending tests were performed according to EN 1015-11:2019 (2019). The mean values obtained were $f_{b,f}=0.30$ MPa and $f_{b,c}=1.56$ MPa (Table 1).

The bricks in the samples were arranged in two different bond patterns. The former (type B1; see Fig. 1a) followed the “English bond” method, with alternating courses of headers and stretchers, the headers centred over the stretchers in the course below. The latter (type B2; see Fig. 1b) replicated a double-leaf masonry wall composed of two adjacent, independent leaves in the “stretcher bond” style, with headers at the ends of alternating rows. Both masonry types had a total thickness of 250 mm.

For each masonry type, monotonic compressive tests were carried out on two masonry wallets (dimensions $500 \times 250 \times 1010$ mm³), according to EN 1052-1:1998 (1998). The main results are reported in Table 2, from which it can be seen that very similar mean values for both the compressive strength (6.70 and 6.43 MPa) and Young’s modulus (2.3 and 2.2 GPa) were obtained for B1 and B2, respectively.

One “H”-shaped masonry sample was built for each masonry type, representing the portion of wall in the spandrel area of actual walls (Fig. 1c). The samples were 2155 mm high and 3890 mm wide (Fig. 1a and b). The outer masonry piers were 1420 mm wide, and the spandrel had a width of 1050 mm and a height of 1095 mm. At the spandrel intrados, a masonry jack arch was created using brick couples arranged alternatively as headers and stretchers (with a height of 250 mm).

The samples were first tested in their unstrengthened state, for reference, up to the occurrence of significant damage (significant load decrease after peak load, with clear evidence of the failure mechanism governing the collapse). They were then repaired and strengthened, and tested again. The sample names used consisted of three parts separated

Table 1 Mechanical properties of the masonry mortar, with their respective coefficients of variation (CoVs)

Property	n° of tests	Mean (MPa)	CoV (–)
Flexural tensile strength, $f_{b,f}$	12	0.30	0.11
Compressive strength, $f_{b,c}$	12	1.56	0.09

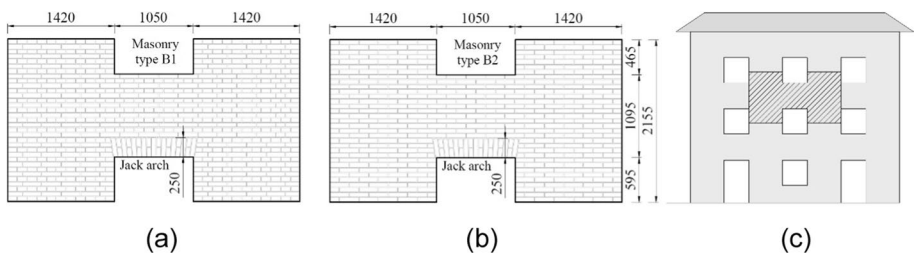


Fig. 1 H-shaped masonry samples for the spandrel tests (all measurements in millimetres): geometric details for **a** sample S-B1 and **b** sample S-B2 and **c** example of sampling in a wall

Table 2 Mechanical properties of the masonry samples obtained from monotonic compressive tests on wallets, in terms of compressive strength ($f_{m,c}$) and Young’s modulus (E_m)

Sample	n°. of tests	$f_{m,c}$ (MPa)	E_m (MPa)
B1	2	6.70	2341.1
B2	2	6.43	2183.3

by a hyphen, the first part indicating the type of test (S for spandrel test), the second the type of masonry (B1 or B2 for single- or double-leaf masonry, respectively), and the third distinguishing between the unreinforced (U) and retrofitted (R) configuration.

To repair the damage from testing the unstrengthened samples, the cracks were injected with a rapid-setting, thixotropic cementitious grout (Fig. 2a). The samples were then strengthened by applying the CRM system to one side. In the single-leaf sample (S-B1), the masonry surface was first cleaned using a wire brush and the mortar in the joints was removed to a depth of about 10–15 mm. Transverse holes, 16 mm in diameter, were drilled in the masonry ($6/m^2$) to a depth of 220 mm, and cleaned of dust (Fig. 2b). A GFRP mesh (with a grid pitch of $66 \times 66 \text{ mm}^2$) was placed over the entire wall surface (Fig. 2c) and L-shaped GFRP connectors were arranged in the holes before fully injecting them with a vinylester chemical anchor. On top of the main mesh, additional pieces of smaller mesh (with a side length of 150 mm and grid spacing of $33 \times 33 \text{ mm}^2$) were placed over the connectors to improve their anchoring (Fig. 2d). Finally, the masonry surface was wetted and a 30-mm-thick mortar coating was applied, taking care to position the mesh at about the middle of the thickness, so that it was completely embedded in the mortar (Fig. 2f).

In the double-leaf sample (S-B2), the CRM system was coupled with additional transverse connectors (diatones). In fact, previous experiences (e.g. Gattesco et al. 2015, 2023b) evidenced the possible activation of leaves separation in CRM strengthened masonry walls, due to the significant increase of the masonry resistance and, thus, of stresses among leaves. An effective connection of leaves is necessary to ensure the best CRM exploitation. To locate the diatones, 50-mm-diameter holes were drilled and a 16-mm-diameter threaded rod (stainless steel AISI 304) was placed in the centre of each hole, which was then injected with a thixotropic, shrinkage-compensated cementitious mortar (the compressive strength provided in the technical sheet was 55 MPa at 28 days). A steel washer, provided with a nut welded in the centre, was screwed to the head of the rod, over diffuse GFRP mesh (Fig. 2e). The washer (stainless steel AISI 304) had a diameter of 150 mm and a thickness of 4 mm, and had several holes in it to promote its embedment within the mortar coating. The positioning of the GFRP connectors and artificial diatones is schematised in Fig. 3a and b. The density of the GFRP connectors was $4/m^2$ and $2/m^2$ for the diatones, giving a total density of connectors of $6/m^2$.

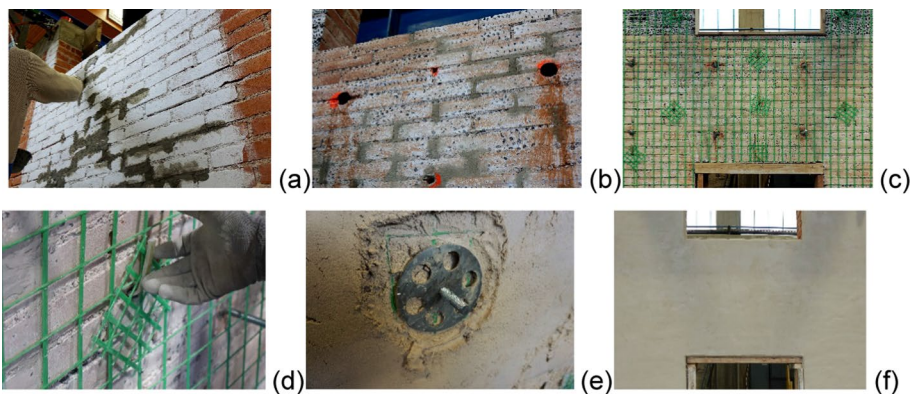


Fig. 2 Strengthening procedure of previously tested masonry: **a** filling of cracks by injection; **b** drilling holes; **c** positioning GFRP mesh; **d** positioning GFRP connectors and **e** artificial diatones; and **f** applying mortar coating

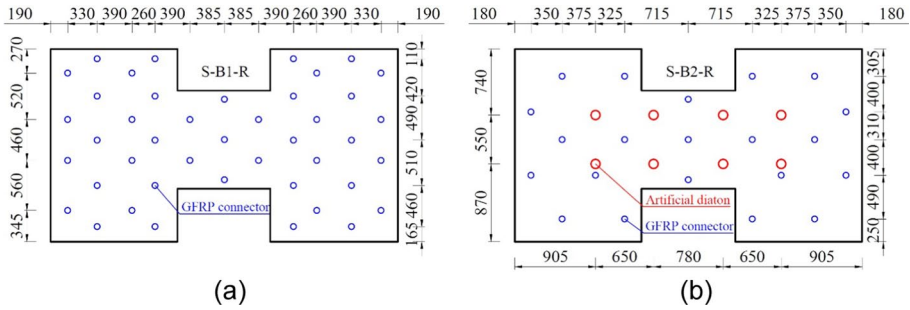


Fig. 3 Transverse connections scheme in the strengthened configurations (all measurements in millimetres): **a** sample S-B1-R and **b** sample S-B2-R

The GFRP mesh was composed of long, alkali-resistant, glass-fibre yarn (with a cross-section of 3.8 mm^2), impregnated with a thermosetting vinylester epoxy resin and woven in a regular square pitch. Direct tensile tests (tensile strength $[T_w]$, axial stiffness $[EA_w]$ and ultimate strain $[\epsilon_u]$) were performed to assess its main mechanical properties, according to EAD 340392-00-0104 (2018) and ISO 10406-1:2015 (2015). The main results are presented in Table 3.

The L-shaped GFRP connectors were also produced by the impregnation of long, alkali-resistant glass-fibre yarns with a thermosetting vinylester epoxy resin. The nominal dimensions of the two main sides were 100 and 200 mm, and the gross cross-section was $7 \times 10 \text{ mm}^2$. The technical sheet provided a dry-fibre cross-section of 32.4 mm^2 and an average tensile strength of 455 MPa.

The mortar used for the coating was a premixed compound-based lime and hydraulic binder. The main mechanical properties are reported in Table 4, the flexural ($f_{c,f(p)}$) and compressive ($f_{c,c(p)}$) strengths having been determined by testing $40 \times 40 \times 160\text{-mm}^3$ prismatic coupons, following EN 1015–11:2019 (2019).

Table 3 Main mechanical characteristics (tensile resistance— T_w , axial stiffness— EA_{tot} and ultimate strain— ϵ_u) of the GFRP wires with their respective CoVs

Characteristic	Parallel-fibre wire		Twisted-fibre wire	
	Mean	CoV (%)	Mean	CoV (%)
T_w (kN)	5.93	3.9	5.11	2.4
EA_{tot} (kN)	291.2	1.6	276.7	2.6
ϵ_u (–)	2.03	4.2	1.85	1.9

Table 4 Mechanical properties of the mortar of the coating (flexural strength— $f_{c,f(p)}$, and compressive strength— $f_{c,c(p)}$, measured on prisms) with their respective CoVs

Property	n° of tests	Mean (MPa)	CoV (–)
Flexural tensile strength, $f_{c,f}$	27	5.0	13.5%
Compressive strength, $f_{c,x}$	27	22.1	10.7%

3 Test setup

The test apparatus (Fig. 4) consisted of two independent, horizontal steel beams (length=3000 mm, labelled with (2) in Fig. 4d), lined up at a distance of 400 mm, placed on support clevis joints with pin, 2470 mm apart. The joints (3) allowed the potential to carry loads in both compression and tension and were equipped with a loading cell at the top—labelled “ C_{Ls} ” and “ C_{Rs} ” in Fig. 4d (± 500 kN capacity). The clevis joints (Fig. 4b, c) allowed free rotation in the plane of the samples. Moreover, at the base of the right joint (Fig. 4c), a couple of parallel bearing rails were added, allowing in-plane horizontal translations, which were measured by a potentiometer transducer fixed to the laboratory floor (h_R in Fig. 4d).

Each pier in the H-shape masonry sample was positioned on one of the steel beams, centred on the knuckle joint. Two servo-hydraulic actuators (250 kN capacity, ± 200 mm stroke, (8)), oriented vertically, were attached to the free, external ends of the steel beams and locked on independent steel frames (7). Loading cells located between the actuators and the beams measured the applied load (C_{Lp} and C_{Rp} in Fig. 4d). Four more hydraulic actuators (500 kN capacity, (9)) were installed on the piers for applying an axial compressive load. On top of these actuators were steel elements (10) connected to the steel beams at the base of the testing apparatus by threaded rods (11). The four actuators were connected in parallel and produced a constant force, which was measured by a pressure transducer (global vertical load of 235 kN, corresponding to a mean

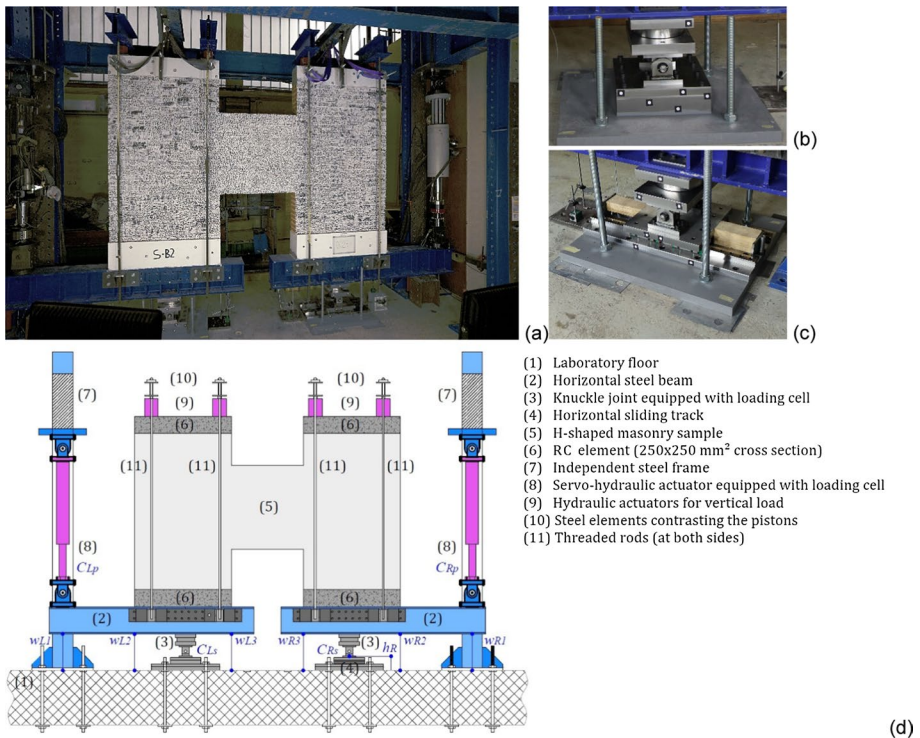


Fig. 4 Test setup: a, b, c photographic illustrations and d schematic, showing the instrumentation

compressive stress of 0.33 MPa). This reproduced typical axial stress in the masonry piers in actual buildings.

During the tests, the two external actuators were moving at the same speed, in opposite directions, which induced equal rotations of the piers ($\theta_L = \theta_R = \theta$ in Fig. 5a). This caused shear and bending actions on the spandrel. The load was applied cyclically in the positive (clockwise rotation of the beams) and negative (anticlockwise rotation) directions, the target rotation amplitude gradually increasing and three repetitions performed for each (Fig. 5b).

The testing apparatus and load pattern basically reproduced those designed by Beyer and Dazio (2012). The main difference stood in the absence of the horizontal rods introducing an axial force into the spandrel. In fact, the tests were specifically carried out to detect the coupling effect of the spandrel due to the CRM application, not influenced by any other horizontal constrain; any tying effect would have reasonably increased the sample performances. In addition to the reference approach, RC elements (cross-section of $250 \times 250 \text{ mm}^2$) were positioned at the base and top of each masonry pier of the sample ((6) in Fig. 4d), to facilitate a uniform load distribution and transfer during testing. Furthermore, three repetitions for each target cycle were performed, instead of the two. Other differences, for example in the sample size and in the length of the lever beams, did not conceptually affect the approach.

A series of six potentiometer transducers (labelled “w” in Fig. 4d) were fixed to the laboratory floor in order to measure the vertical displacements at the intrados of the two beams at different positions, which corresponded to the external actuators and the outer and inner corners of the masonry columns.

The instruments were connected to an electronic acquisition unit interfaced with a computer, allowing the real-time monitoring of the forces and displacements during the test. In addition, a Digital Image Correlation (DIC) system (Howlader et al. 2021; Oats et al. 2022) was used for monitoring the entire displacement fields at the front face of the sample. A pair of cameras was used to obtain a three-dimensional position, using the same principle as the stereo vision in humans. A random speckled pattern was painted on the front wall surface to facilitate identification of the same measurement points in pictures taken from both cameras.

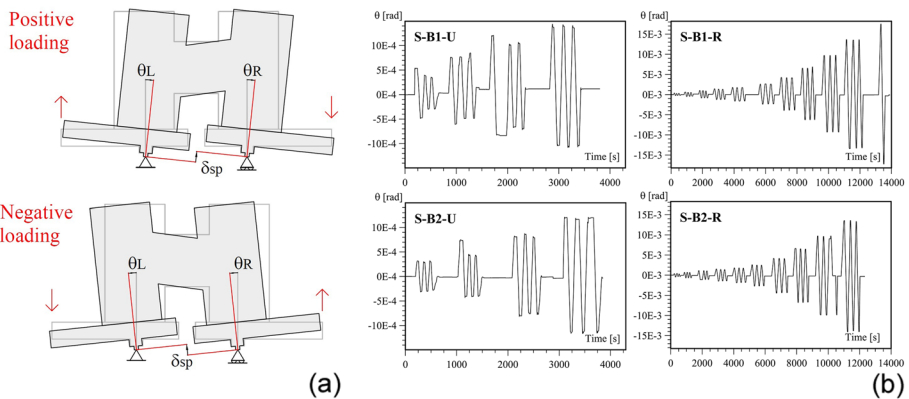


Fig. 5 Sample loading: a loading directions; and b loading protocol

4 Results

The spandrel response was observed in terms of capacity curves representing the shear load (V_{sp}) as a function of spandrel distortion (δ_{sp}) or drift (γ_{sp}). The shear load (V_{sp}) was obtained from the vertical translation equilibrium of the external vertical forces acting on the left half (or, similarly, on the right half) of the sample; that is, the load applied by the outer actuator C_{Lp} (or C_{Rp}) and the reaction at the support C_{Ls} (or C_{Rs}).

$$V_{sp} = C_{Lp} + C_{Ls} = C_{Rp} + C_{Rs} \quad (1)$$

The vertical distortion (δ_{sp}) effectively applied to the spandrel was the base rotation (θ) multiplied by the distance ($d=2470$ mm) between the knuckle joints. The rotation was the sum of the vertical displacements ($w_{L2}+w_{L3}$ or, similarly, $w_{R3}+w_{R2}$) divided by the column width ($s=1420$ mm).

$$\delta_{sp} = \theta \cdot d = \frac{(w_{L2} + w_{L3})}{s} \cdot d = \frac{(w_{R3} + w_{R2})}{s} \cdot d \quad (2)$$

The spandrel drift (γ_{sp}) was determined by dividing the vertical distortion (δ_{sp}) by the spandrel's length (1050 mm).

The principal tensile strain field monitored through the DIC system was particularly useful for observing crack development in the spandrels. It was particularly interesting to compare the crack patterns with the attainment of first cracking (Cr), peak load (Pk) and near collapse (Nc). This latter was assumed to have been attained for a 30% shear load decrease from the peak load. The expected failure mechanisms in spandrels are those typical of historic masonry (diagonal cracking, bending and shear-sliding), except that the cracks indicative of bending and shear-sliding were vertical at the ends of the spandrels.

The unstrengthened masonry samples were tested about 35 days after construction. Then, they were tested again about 5 weeks after the strengthening intervention.

4.1 Single-leaf masonry (S-B1)

The evolution of the crack pattern in the single-leaf, unstrengthened masonry spandrel (sample S-B1-U) is shown in Fig. 6, and the capacity curves ($V_{sp}-\delta_{sp}$ or $V_{sp}-\gamma_{sp}$) are illustrated in Fig. 7a. The first cracks occurred at the ends of the jack arch, first at the left corner of the spandrel (Fig. 6a), when loading in the positive direction ($V_{sp} = +22.9$ kN at $\delta_{sp} = +1.14$ mm), and then suddenly also in the right corner (Fig. 6b), when loading in the negative direction ($V_{sp} = -26.8$ kN at $\delta_{sp} = -1.02$ mm). When reaching peak load (+26.6 and -30.6 kN, +1.85/-1.45 mm), cracks also formed around the top corners of the spandrel, leading to activation of the bending failure mechanism (Fig. 6b and c). The upper cracks then opened with an inclined trend, the lower ones almost vertically, and the load correspondingly rapidly dropped to the near-collapse condition, which was achieved shortly after, at +2.84/-2.03 mm (Fig. 6e and f). A horizontal crack in the top corners of the jack arch was also observed. As the cracks extended over the entire spandrel height, the right pier began to move away horizontally. The movement was independent of the loading direction, as can be seen in the $V_{sp}-\delta_h$ curve in Fig. 7b. At the end of the test (Fig. 6g and h), the arch was completely surrounded by cracks and imminently about to fall. The residual horizontal sliding reached 2.8 mm. The damage pattern detected on the back of

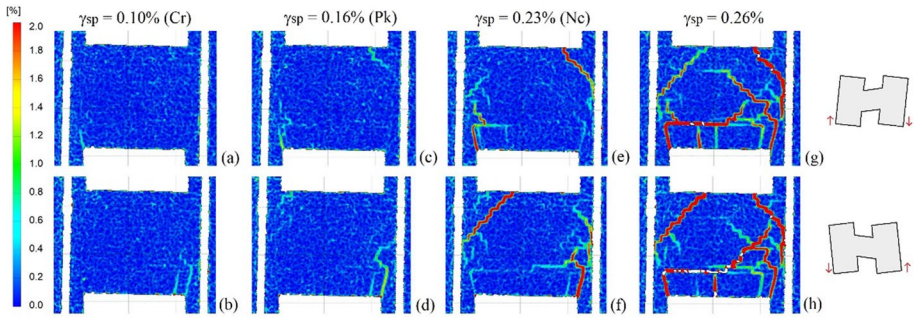


Fig. 6 Sample S-B1-U: crack evolution obtained by the DIC system, when loading in the **a, c, e, g** positive and **b, d, f, h** negative direction. The sub-plots refer to the attainment of **a, b** first cracking, **c, d** peak load, **e, f** near collapse and **g, h** end of the test

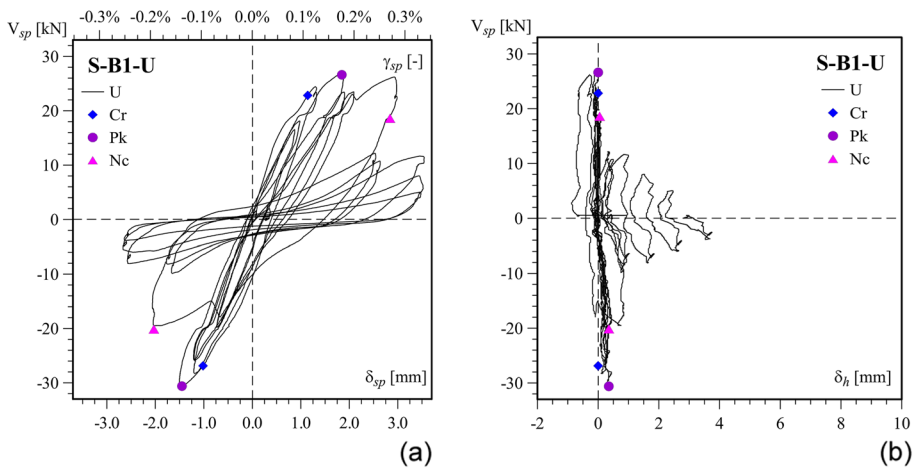


Fig. 7 Sample S-B1-U curves of: **a** $V_{sp}-\delta_{sp}$ (or $V_{sp}-\gamma_{sp}$); and **b** $V_{sp}-h_h$

the wall was the same as on the front, with cracks running almost exclusively through the mortar joints.

The unstrengthened sample (S-B1-U) has been repaired and strengthened, and then tested again (S-B1-R). The crack pattern evolution and the capacity curve for the single-leaf, strengthened masonry sample S-B1-R, are shown in Figs. 8, 9 and 10a, respectively. Cracks in the coating were first observed in the bottom-left corner of the spandrel, at $V_{sp} = -23.2$ kN ($\delta_{sp} = -0.26$ mm; see Fig. 8b), and then in the bottom-right corner, at $V_{sp} = +19.6$ kN ($\delta_{sp} = +0.77$ mm; see Fig. 8a). Then, cracks also opened in the top corners (Fig. 8c and d), indicating activation of a bending mechanism, similarly to that in the unstrengthened configuration. However, this time, the cracks did not cause failure due to the GFRP wires in the cracks still providing resistance. As the spandrel distortion increased, the shear force continued to increase despite the reduction in stiffness. The cracks at the edges were almost vertical, but other cracks gradually occurred in the vicinity. These cracks developed towards the centre of the spandrel and became gradually more inclined (Fig. 8e and f). When peak load was achieved ($V_{sp} = +38.9/-37.4$ kN at $\delta_{sp} = +16.3/-13.4$ mm), the entire coating was diffusely covered with cracks,

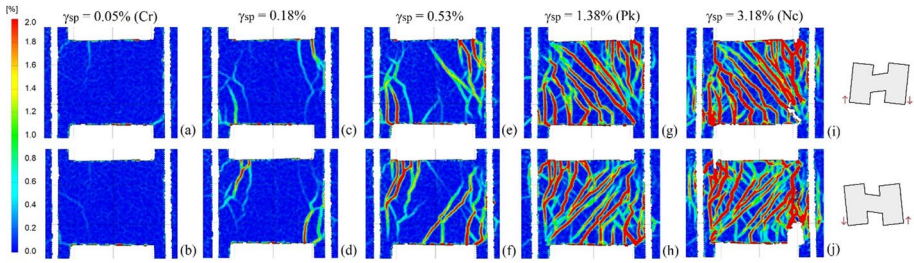


Fig. 8 Sample S-B1-R: crack evolution in the coating obtained by the DIC system, when loading in the **a, c, e, g, i** positive and **b, d, f, h, j** negative direction. The sub-plots refer to the attainment of **a, b** first cracking, **c, d** drift 0.18%, **e, f** drift 0.53%, **g, h** peak load and **i, j** near collapse

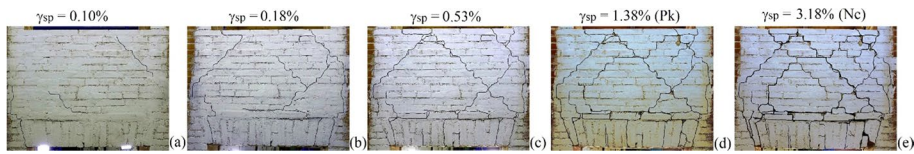


Fig. 9 Sample S-B1-R: crack pattern evolution on the unstrengthened side of the wall. The sub-plots refer to the attainment of **a** drift 0.10%, **b** drift 0.18%, **c** drift 0.53%, **d** peak load and **e** near collapse

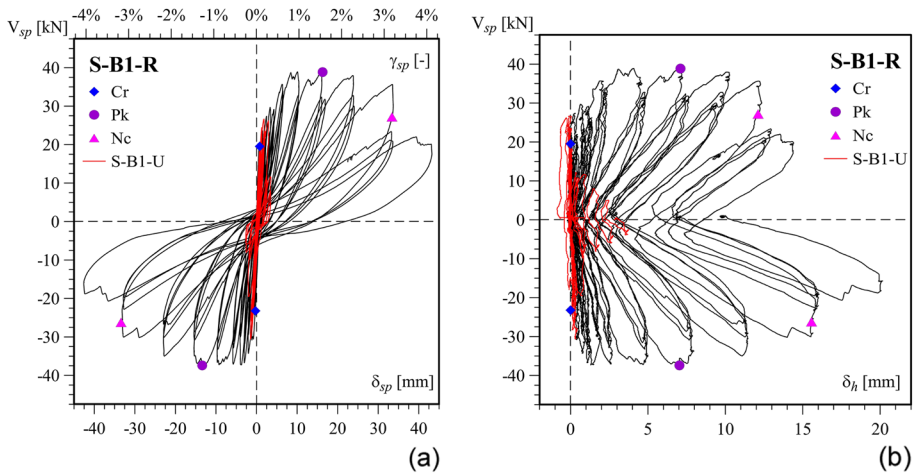


Fig. 10 Sample S-B1-R curves of: **a** $V_{sp}-\delta_{sp}$ (or $V_{sp}-\gamma_{sp}$); and **b** $V_{sp}-h_R$. The curves of S-B1-U appear in red for comparison

and the cracks at the centre of the spandrel were diagonal (Fig. 8g and h). This was followed by a gradual decrease in strength until the near-collapse condition was achieved at $\delta_{sp} = \pm 33.4$ mm (Fig. 8i and j), when the horizontal GFRP wires at the right end of the spandrel progressively failed in tension, starting from the bottom corner (Fig. 11). No out-of-plane bending or swelling phenomena were detected during the test. It should be noted that the bond between the coating and the spandrel was lost in the cracked areas, but the anchors and the diatones maintained composite action until the end.

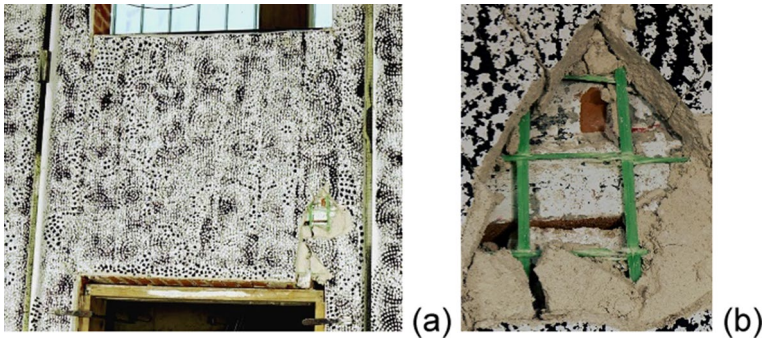


Fig. 11 Sample S-B1-R: tensile failure of the GFRP horizontal wires at the bottom right corner at the end of the test, in **a** global spandrel view and **b** detail

The evolution of the damage on the unstrengthened side (Fig. 9) showed a gradual wide-spread development of inclined cracks mainly running through the joints over the entire spandrel. There were fewer cracks on the unstrengthened side, and these were very similar to those observed in the test of the unstrengthened spandrel, S-B1-U (compare Fig. 9e with Fig. 6g and h). The large crack above the jack arch opened again, but the arch was held in position by the CRM on the rear face.

The base horizontal displacement (δ_h) (Fig. 10b) showed the progressive moving away of the right pier (about 7 mm at peak load and 14 mm at near collapse), with a residual sliding at the end of the test of about 10 mm.

4.2 Double-leaf masonry (S-B2)

The damage evolution of the double-leaf, unstrengthened masonry configuration, S-B2-U, is shown in Fig. 12 and the capacity curve ($V_{sp}-\delta_{sp}$ or $V_{sp}-\gamma_{sp}$) in Fig. 13a. The

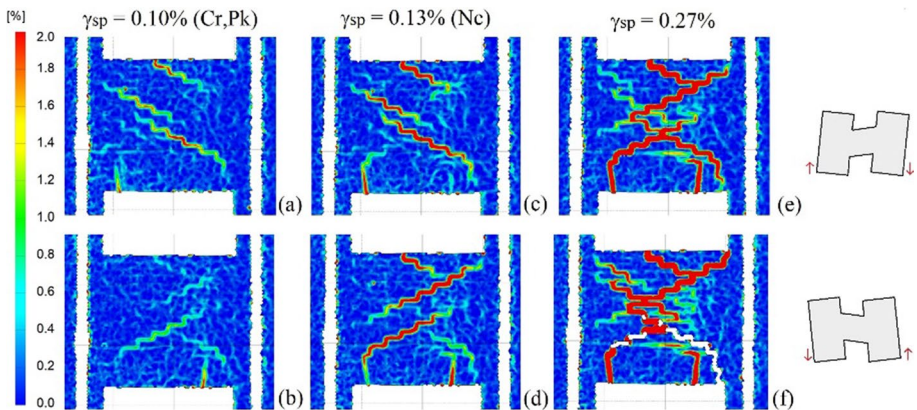


Fig. 12 Sample S-B2-U: crack evolution obtained by the DIC system, when loading in the **a, c, e** positive and **b, d, f** negative direction. The sub-plots refer to the attainment of **a, b** first cracking—corresponding also to the peak load, **c, d** near collapse and **e, f** end of the test

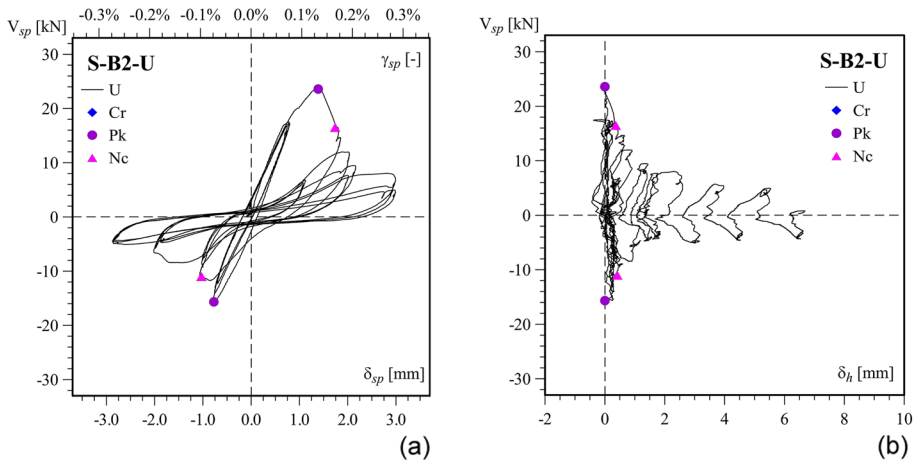


Fig. 13 Sample S-B2-U curves showing: **a** $V_{sp}-\delta_{sp}$ (or $V_{sp}-\gamma_{sp}$); and **b** $V_{sp}-l_h$

first significant cracking coincided with attainment of the peak load, at $V_{sp} = +23.6$ kN ($\delta_{sp} = +1.39$ mm; see Fig. 12a) and -15.7 kN ($\delta_{sp} = -0.77$ mm; see Fig. 12b). At this stage, the cracks were inclined, running mostly through the joints. This pattern is indicative of the diagonal shear failure mechanism. The resistance decay was immediate and the near collapse was achieved at $\delta_{sp} = +1.74/-1.03$ mm (Fig. 6b and c). The cracks opened wide, which resulted in large horizontal slidings at the base of the right pier, as illustrated in Fig. 13b (the residual sliding was $\delta_h = +6.5$ mm). This caused the lower portion of the masonry spandrel, which was fully surrounded by cracks, to detach from the upper portion at the end of the test ($\delta_{sp} = \pm 2.8$ mm; see Fig. 12e and f). The crack pattern was identical on both sides of the sample.

The damage evolution of the strengthened double-leaf brick masonry sample S-B2-R, is shown in Figs. 14 and 15 and its capacity curve in Fig. 16a. The first cracks in the coating occurred at diagonally opposite corners of the spandrel, at $V_{sp} = +21.6$ kN ($\delta_{sp} = +0.92$ mm see Fig. 14a) and at $V_{sp} = -23.8$ kN ($\delta_{sp} = -1.1$ mm; see Fig. 14b). The cracks progressively spread over the spandrel. They were initially almost vertical, but, at about $\delta_{sp} = \pm 2.8$ mm, diagonal cracks appeared in the centre of the spandrel (Fig. 14c and d), at which point, there was also a visible reduction in stiffness of the capacity curve.

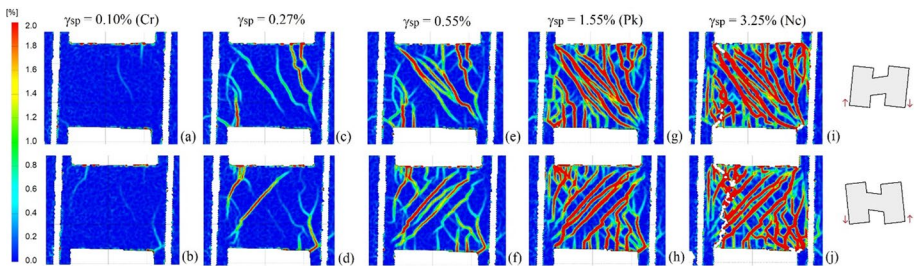


Fig. 14 Sample S-B2-R: crack evolution in the coating obtained by the DIC system, when loading in the **a, c, e, g, i** positive and **b, d, f, h, j** negative direction. The sub-plots refer to the attainment of **a, b** first cracking, **c, d** drift 0.27%, **e, f** drift 0.55%, **g, h** peak load and **i, j** near collapse

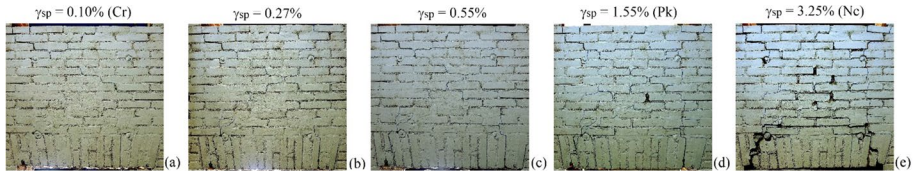


Fig. 15 Sample S-B2-R: crack pattern evolution on the reverse side of the wall

Horizontal sliding at the base of the right pier (δ_h) was also activated (Fig. 16b). The parallel diagonal cracks then gradually spread over the coating (Fig. 14e and f) and, when peak load was reached, at $V_{sp} = +45.5$ kN ($\delta_{sp} = +16.0$ mm; see Fig. 14g) and $V_{sp} = -42.7$ kN ($\delta_{sp} = -16.5$ mm; see Fig. 14h), the cracks in the coating covered the entire spandrel surface. On the reverse side (unstrengthened masonry), the cracks also gradually diffused (Fig. 15), but the trend was that of stepped cracking that mainly followed previously repaired cracks. Figure 15e clearly shows detachment of the lower spandrel portion, similar to what happened in the unstrengthened configuration (Fig. 12e and f). However, this was not observed in the coating on the other side, and the falling of the jack arch was thus effectively prevented.

No layer separation, induced by parasitic out-of-plane bending or swelling phenomena, were found, either between the wall leaves or between the masonry and the coating. Throughout the testing, the deformations were concentrated along vertical cracks around the sides of the spandrel, apart from the inclined cracking that indicates shear damage. However, the final collapse was due to tensile failure of some vertical GFRP wires (Fig. 17b), reminiscent of vertical shear sliding. A mortar strip along the failure line was crushed and fell off (Fig. 17a).

The base horizontal displacement (δ_h) (Fig. 16b) was about 6.7 and 12 mm at peak load and near-collapse, respectively. The residual slip was 2.9 mm.

5 Comparison and analysis of results

The main results obtained from the four tests are summarised in Table 5, and a visual comparison of the peak loads and ultimate drifts is provided in Fig. 18. As might have been expected, the single-leaf brick masonry (S-B1-U) performed better, in terms of both strength and displacement capacity, compared to the double-leaf masonry (S-B2-U) due to the interconnection of the leaves. The failure mechanisms were also different, with the single-leaf masonry spandrel failing by bending and the double-leaf spandrel by diagonal shear. However, both samples responded in a very brittle fashion with very limited ultimate drifts (0.13–0.23%). The double-leaf spandrel performed worse in this category as well.

The resistance and displacement capacity at first cracking were relatively comparable in the unstrengthened and strengthened configurations, with the sealing of the cracks and the application of CRM approximately restoring the initial integrity of the samples. Comparable results were obtained from the two strengthened configurations, with a mean peak resistance of 38.1 kN for S-B1-R and 44.1 kN for S-B2-R, and similar drifts at peak load (1.38–1.55%) and at near collapse (3.18–3.25%). This seems to indicate that the masonry bond had a limited influence on the behaviour of the strengthened samples. The GFRP mesh embedded in the plaster provided the spandrels with tensile strength, which

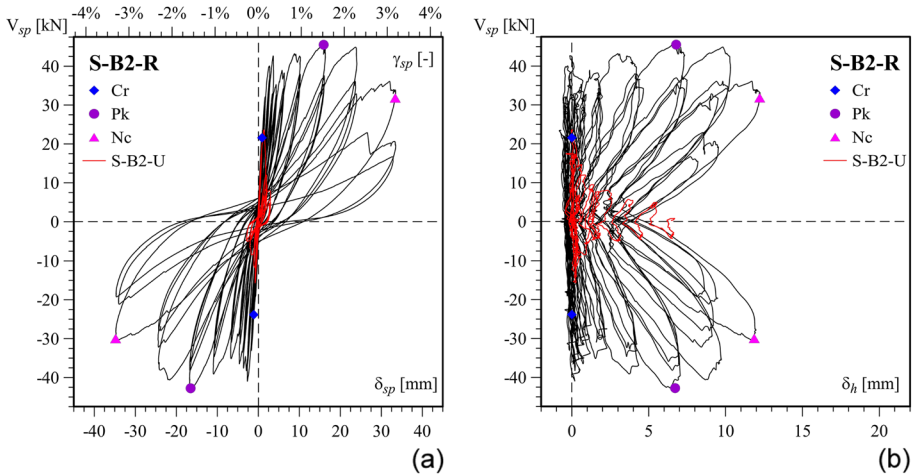


Fig. 16 Sample S-B2-R curves of: **a** $V_{sp}-\delta_{sp}$ (or $V_{sp}-\gamma_{sp}$); and **b** $V_{sp}-h_R$. The curves of S-R2-U appear in red for comparison

fundamentally changed the damage evolution compared to the unstrengthened configurations. Whereas in the unstrengthened samples, a few wide cracks opened, in the strengthened samples, there was a wide diffusion of several narrower cracks. The diffuse cracking was key to the increased energy dissipation. In both strengthened samples, the first cracks in the coating were vertical at the sides, indicating bending. This was followed by the occurrence of inclined cracks in the panel. On the unstrengthened side, the cracks tended to reproduce the original damage pattern, which consisted of predominantly inclined cracks. However, the final collapse mechanisms were different, with the coating failing in a bending-dominated way in S-B1-R, with the fracturing of horizontal GFRP wires, whereas the vertical wires fractured in S-B2-R. Crucially, in both cases, the anchors maintained composite action of the coating and masonry until the collapse, although the actual bond (contact) was lost over large areas.

Significant gains, in terms of both strength and displacement capacity, were provided. For the single-leaf sample, S-B1-R, the peak strength was 33% greater than for S-B1-U at a drift more than 8.8 times higher. The drift capacity at near collapse was 13.7 times higher.

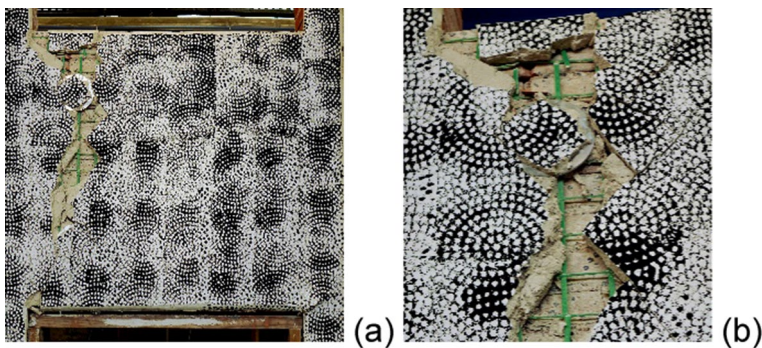


Fig. 17 Sample S-B2-R: tensile fracture of the vertical wires of GFRP on the left side of the spandrel at the end of the test in **a** global spandrel view and **b** detail

Table 5 Spandrel shear force (V_{sp}), distortion (δ_{sp}), drift (γ_{sp}) and horizontal sliding at the right support (h_R) in positive and negative loading directions for the first cracking, peak load and near collapse limit states

Sample	First cracking, F_c			Peak load, P_k			Near collapse, N_c			
	V_{sp} (kN)	δ_{sp} (mm)	γ_{sp} (-) (%)	V_{sp} (kN)	δ_{sp} (mm)	γ_{sp} (-) (%)	V_{sp} (kN)	δ_{sp} (mm)	γ_{sp} (-) (%)	h_R (mm)
S-B1-U	22.9	1.14	0.109	26.6	1.85	0.176	18.6	2.84	0.270	0.05
	-26.8	-1.02	-0.097	-30.6	-1.45	-0.138	-20.1	-2.03	-0.193	0.35
S-B1-R	19.6	0.77	0.074	38.9	16.3	1.516	27.2	33.4	3.181	12.12
	-23.2	-0.26	-0.024	-37.4	-13.4	-1.246	-26.2	-33.4	-3.181	15.57
S-B2-U	23.6	1.39	0.132	23.6	1.39	0.132	16.5	1.74	0.166	0.36
	-15.7	-0.77	-0.074	-15.7	-0.77	-0.074	-11.0	-1.03	-0.098	0.41
S-B2-R	21.6	0.92	0.087	45.5	16.0	1.519	31.9	33.4	3.181	12.22
	-23.8	-1.10	-0.105	-42.7	-16.5	-1.572	-29.9	-34.8	-3.314	11.86

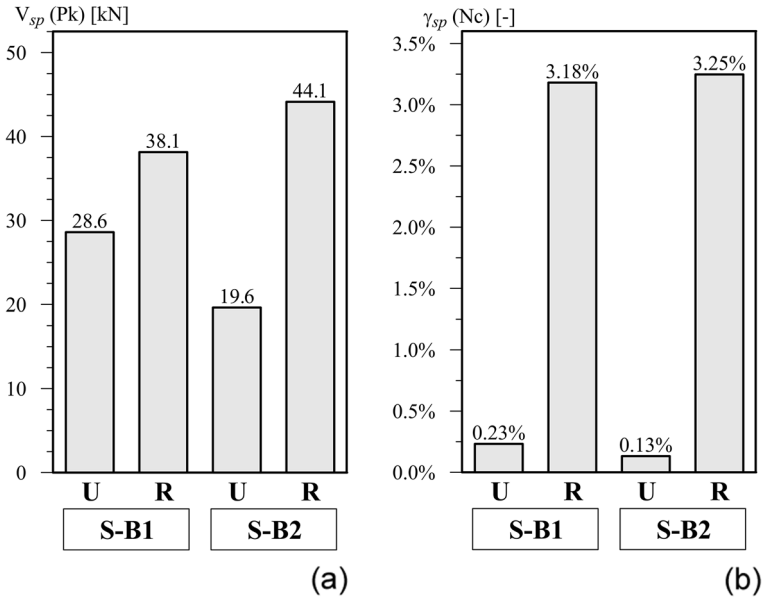


Fig. 18 Comparison between unstrengthened (U) and strengthened (R) spandrels in terms of: **a** peak load; and **b** ultimate drift

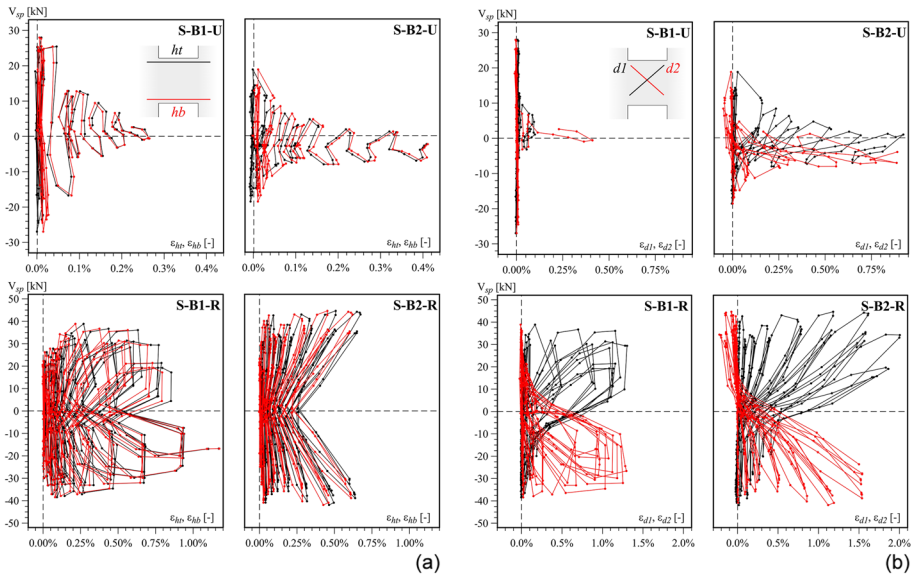


Fig. 19 Evolution of strains monitored through the DIC system: **a** horizontal; and **b** diagonal

In the two-leaf masonry sample, S-B2-R, the peak force was more than doubled, with a 125% increase compared to S-B2-U at a drift more than 15 times higher. The drift capacity at near collapse was 24.6 times higher. In general, the CRM one-side application allowed

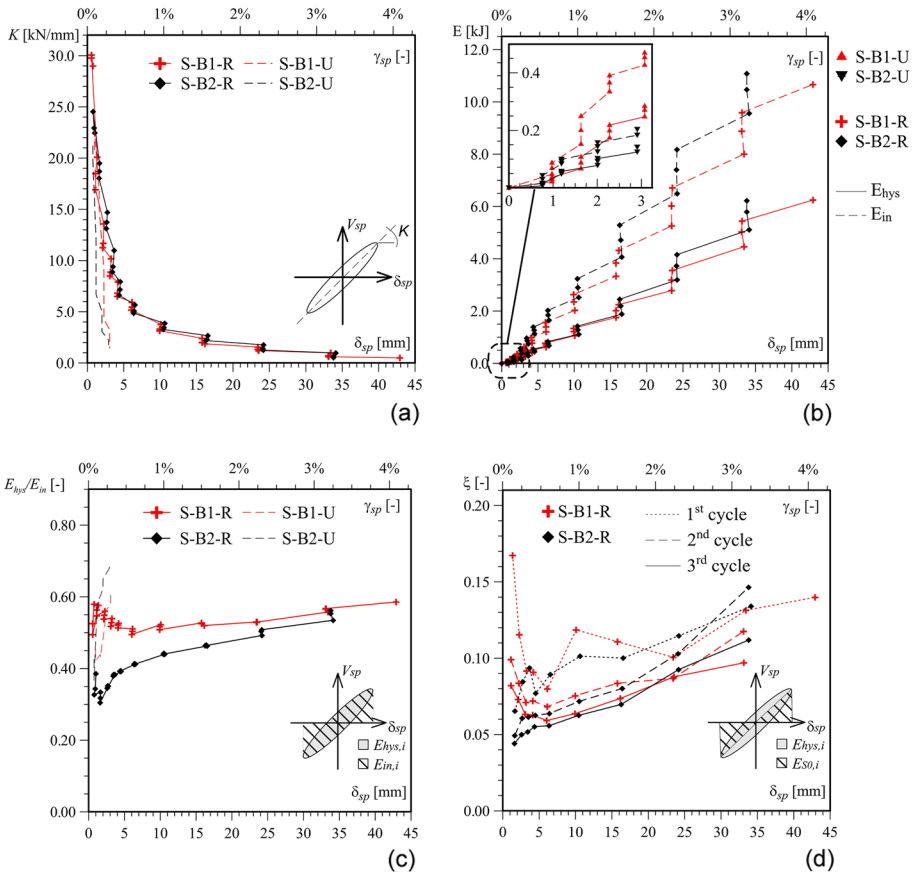


Fig. 20 **a** Cycle stiffness; **b** cumulative dissipated E_{hys} and total E_{in} energies; **c** E_{hys}/E_{in} ratio; and **d** equivalent hysteretic damping ξ_{hys} for each cycle of the strengthened samples

the attainment of drift values one order of magnitude higher than plain masonry, roughly in line with similar spandrels provided with an effective horizontal tie (Gattesco et al. 2016; Beyer and Dazio 2012).

Although coarser than the acquisitions from the potentiometric transducers, the DIC system allowed an analysis of the equivalent strain evolution in the spandrel area and, in particular, those related to the horizontal deformation at top and bottom (ϵ_{ht} , ϵ_{hb}) and along the diagonals (ϵ_{d1} , ϵ_{d2}) (Fig. 19). The base lengths were about 1800 and 700 mm, respectively. Consistently with the crack pattern, the top and bottom horizontals stretched almost simultaneously (Fig. 19a), the diagonals alternately ($d2$ for positive loading, $d1$ for negative; see Fig. 19b). A comparison between the $V_{sp}-\epsilon_d$ plots of S-B1-U and S-B2-U clearly shows failure dominated by diagonal cracking in the latter test, instead of the bending-dominated failure that occurred in the former. Significantly higher strain values were generally attained by the retrofitted configurations. The strains in the $V_{sp}-\epsilon_h$ graphs were slightly wider for sample S-B1-R than S-B2-R, while those in the $V_{sp}-\epsilon_d$ graphs were wider for S-B2-R.

Table 6 Values of cumulative input energy (E_{in}) and dissipated hysteresis (E_{hys}) at resistance peak (Pk) and near collapse (Nc), and mean cumulative energy ratio in the cycles (E_{hys}/E_{in})

Sample	E_{in} (J)		E_{hys} (J)		E_{hys}/E_{in} (-)	
	Pk	Nc	Pk	Nc	Pk	Nc
S-B1-U	152.3	334.6	66.8	174.0	0.44	0.52
S-B1-R	3333.4	8006.4	1757.2	4463.2	0.53	0.56
S-B2-U	83.8	125.2	48.2	77.9	0.58	0.62
S-B2-R	4069.1	9560.2	1883.4	5109.7	0.46	0.53

6 Stiffness and energy content

The decreasing trends in effective cyclic stiffness are illustrated in Fig. 20a, where K is the stiffness evaluated as the slope of the peak-to-peak line within each loop of the capacity curve. The $K-\delta_{sp}$ curves exhibit an exponential decrease, their final values being less than 10% of the initial values. Although the values of the unstrengthened and strengthened samples were initially comparable (within a range of 21–30 kN/mm), a more gradual degradation occurred in the strengthened samples. The stiffness gap within the three loops of a single target displacement was quite low.

The amount of cumulative input energy (E_{in}) and the dissipated hysteretic energy (E_{hys}) were evaluated. For the i -th cycle, $E_{hys,i}$ was calculated as the area within the hysteretic loop and $E_{in,i}$ as the area under the positive and negative branches of the loop. The trends in E_{in} and E_{hys} are plotted in Fig. 20b and summarised in Table 6 for the peak and near collapse conditions. The E_{hys}/E_{in} ratios were also calculated and are plotted in Fig. 20c. Based on the lower performance of sample S-B2-U compared to S-B1-U, the input energy and dissipated cumulative energy were also lower (about –36% at peak and –60% at near collapse). The E_{hys}/E_{in} ratios that tended to increase as δ_{sp} increased ranged between 0.45 and 0.61 in S-B1-U and 0.47 and 0.70 in S-B2-U. As expected, the cumulative energies were significantly greater in the strengthened configurations—for B1, the dissipated energy at near collapse increased by 26 times and for B2, by 66 times. The values of E_{hys} were relatively comparable in the two strengthened samples, although slightly lower amounts of E_{in} and higher E_{hys}/E_{in} ratios were observed for S-B1-R. However, as the spandrel drift increased, these values tended to converge (0.46–0.53 at peak load, 0.53–0.56 at near collapse).

For the strengthened samples, an approximate estimation of the equivalent hysteretic damping with varying target displacement was calculated, according to the following equation (Chopra 1995; FEMA440 2005):

$$\xi_{hys} = \frac{E_{hys,i}}{2\pi E_{S0,i}} \tag{3}$$

where $E_{S0,i}$ = strain energy associated with the effective stiffness in each loop.

The trends in ξ_{hys} are reported in Fig. 20d for each of the three cycles at each spandrel target drift. Generally, at a given target drift, the reduction in ξ_{hys} was greater between the second and third cycles than between the first and second. Moreover, the values at peak load (0.10–0.11) and near collapse (0.13) almost coincided with those of S-B1-R and S-B2-R.

7 Conclusions

The behaviour of brick masonry spandrels, and the effect of single-sided strengthening with a CRM coating, was investigated through testing of H-shaped masonry panels. The tests reproduced in a simplified way the in-plane loading conditions experienced by spandrels during earthquake from cyclical rotations of masonry piers.

Two samples were tested in an unstrengthened state. These were then repaired, strengthened with the CRM coating and tested again. The performances were compared in terms of their shear force, distortion (or drift) and energy dissipation capacities. Both samples were 250 mm thick one was single-leaf masonry and the other had two leaves, with both having a jack arch at the spandrel intrados.

The unstrengthened configurations showed a very brittle response, with an abrupt decrease in strength following the opening of a few wide cracks. In the single-leaf masonry, the failure was governed by bending, whereas in the double-leaf masonry, the failure was due to diagonal cracking. Both samples experienced detachment of the jack arch from the upper masonry caused by the coupling of the two masonry piers, provided by the spandrels, being lost once the cracks opened. The residual strength was entirely due to friction among the bricks and was consequently very low.

Filling the cracks first restored the original condition, and then the walls were strengthened using a GFRP mesh–reinforced CRM coating on one side. The capacity of the GFRP mesh to resist tension created a much stronger coupling effect of the spandrel in the piers, which resisted the opening of cracks and facilitated a widespread diffusion but of thinner cracks over the entire spandrel. Moreover, the transverse connectors ensured composite action of the coating and the masonry and prevented leaf separation up to collapse. The GFRP mesh was thus fully utilised, and the final collapse occurred only after the wires of the mesh fractured.

In the single—and double-leaf masonry, the peak resistance was increased by 33% and 125%, respectively. The drifts in the strengthened samples reached 1.5% at peak load and 3.2% at collapse, which is one order of magnitude greater than for the unstrengthened samples. The large increase in displacement capacity was also reflected in the energy dissipation capacity, which increased by 25 and 66 times for the single- and double-leaf masonry, respectively. Around the severe damage stage, the ratio of dissipated energy to input energy was about 50%–55% and the equivalent viscous damping was about 0.10–0.13.

The results proved the effectiveness of the investigated technique for enhancing the in-plane behaviour of historic brick spandrels. Further experimental tests are in progress on different masonry types, such as rubble stone. These original results will be very useful for calibrating numerical models for CRM-strengthened spandrels, as well as for analytical calculations towards the design and performance prediction of CRM-strengthened buildings.

Acknowledgements The experimental tests presented here were carried out as part of the CONSTRRAIN project, funded by the Interreg Italy–Slovenia Cooperation Programme 2014–2020, and led by the University of Trieste (Italy) in cooperation with the University of Ljubljana (Slovenia) and the companies FibreNet S.p.A., Igmata d.d., Veneziana Restauri Costruzioni S.r.l. and Kolektor CPG d.o.o. The support of the Italian Department of Civil Protection (Reluis 2022–2024, WP5) and of the Slovenian Research Agency (project P2-0185) is also gratefully acknowledged.

Author contributions IB, NG and MG were responsible for conceptualising this work and determining the methodology. NG acquired the funding, administered the project and supervised the work. The necessary

resources were obtained by MG and AD. The investigation was carried out by NG, ER, MG and AD. The data were curated by IB, ER and MG, with IB doing the visualisation. The original draft was written by IB, with IB, NG, ER and MG all being involved in reviewing and editing the paper. All authors read and approved the final manuscript.

Funding Open access funding provided by Università degli Studi di Trieste within the CRUI-CARE Agreement. This work was supported by the Interreg Italy–Slovenia Cooperation Programme 2014–2020 (“CON-STRAIN” project), the Italian Department of Civil Protection (Reluis 2022–2024, WP5) and the Slovenian Research Agency (project P2-0185).

Data availability The datasets generated during the current study are available from the corresponding author on reasonable request.

Declarations

Conflict of interest One of the authors, Eng. Allen Dudine, is a collaborator at Fibre NET S.p.A., which manufactures some products related to the research described in this paper. However, Eng. Allen Dudine had no influence over the data collection, analysis, or interpretation. The other authors declare no conflicts of interest.

Open Access This article is licensed under a Creative Commons Attribution 4.0 International License, which permits use, sharing, adaptation, distribution and reproduction in any medium or format, as long as you give appropriate credit to the original author(s) and the source, provide a link to the Creative Commons licence, and indicate if changes were made. The images or other third party material in this article are included in the article’s Creative Commons licence, unless indicated otherwise in a credit line to the material. If material is not included in the article’s Creative Commons licence and your intended use is not permitted by statutory regulation or exceeds the permitted use, you will need to obtain permission directly from the copyright holder. To view a copy of this licence, visit <http://creativecommons.org/licenses/by/4.0/>.

References

- Beyer K, Dazio A (2012) Quasi-static cyclic tests on masonry spandrels. *Earthq Spectra* 28(3):907–929. <https://doi.org/10.1193/1.4000063>
- Chopra AK (1995) Dynamics of structures: theory and applications to earthquake engineering. Prentice Hall, Hoboken. <https://doi.org/10.1002/eqe.4290240809>
- EAD 340392-00-0104 (2018) CRM (composite reinforced mortar) systems for strengthening concrete and masonry structures. European Organisation for Technical Assessment (EOTA), Brussels
- EN 1015-11:2019 (2019) Methods of test for mortar for masonry—part 11: determination of flexural and compressive strength of hardened mortar. Comité Européen de Normalisation (CEN), Brussels
- EN 1052-1:1998 (1998) Methods of test for masonry—part 1: determination of compressive strength. CEN, Brussels
- EN 771-1:2011+A1:2015 (2015) Specification for masonry units—part 1: clay masonry units. Comité Européen de Normalisation (CEN), Brussels
- FEMA440 (2005) Improvement of nonlinear static seismic analysis procedures. Federal Emergency Management Agency (FEMA), Washington
- ISO 10406-1:2015 (2015) Fibre-reinforced polymer (FRP) reinforcement of concrete—test methods—Part 1: FRP bars and grids. International Organization for Standardization (ISO)
- Foraboschi P (2009) Coupling effect between masonry spandrels and piers. *Mater Struct* 42:279–300
- Gattesco N, Boem I (2015) Experimental and analytical study to evaluate the effectiveness. *Constr Build Mater* 88:94–104. <https://doi.org/10.1016/j.conbuildmat.2015.04.014>
- Gattesco N, Boem I (2017a) Characterization tests of GFRM coating as a strengthening technique for masonry buildings. *Compos Struct* 165:209–222. <https://doi.org/10.1016/j.compstruct.2017.01.043>
- Gattesco N, Boem I (2017b) Out-of-plane behavior of reinforced masonry walls: experimental and numerical study. *Compos B Eng* 128:39–52. <https://doi.org/10.1016/j.compositesb.2017.07.006>
- Gattesco N, Amadio C, Bedon C (2015) Experimental and numerical study on the shear behavior of stone masonry walls strengthened with GFRP reinforced mortar coating and steel-cord reinforced repointing. *Eng Struct* 90:143–157. <https://doi.org/10.1016/j.engstruct.2015.02.024>
- Gattesco N, Macorini L, Dudine A (2016) Experimental response of brick-masonry spandrels under in-plane cyclic loading. *J Struct Eng* 142(2):04015146. [https://doi.org/10.1061/\(ASCE\)ST.1943-541X.0001418](https://doi.org/10.1061/(ASCE)ST.1943-541X.0001418)

- Gattesco N, Boem I, Rizzi E, Dudine A, Gams M (2023a) Cyclic tests on two-leaf rubble stone masonry spandrels strengthened with CRM coating on one or both sides. *Eng Struct* 296:116965. <https://doi.org/10.1016/j.engstruct.2023.116965>
- Gattesco N, Rizzi E, Boem I, Dudine A, Gams M (2023b) A new method of seismic strengthening stone masonry with CRM coatings. *Constr Build Mater* 407:133565. <https://doi.org/10.1016/j.conbuildmat.2023.133565>
- Graziotti F, Magenes G, Penna A (2012) Experimental cyclic behaviour of stone masonry spandrels. In: Proceedings of the 15th world conference of earthquake engineering, Lisbon, Portugal
- Graziotti F, Penna A, Magenes G (2014) Influence of timber lintels on the cyclic behaviour of stone masonry spandrels. In: Proceedings of the 9th international masonry conference, Guimarães, Portugal
- Howlader MK, Masia MJ, Griffith MC (2021) Digital image correlation for the analysis of in-plane tested unreinforced masonry walls. *Structures* 29:427–445. <https://doi.org/10.1016/j.istruc.2020.11.051>
- Knox CL, Dizhur D, Ingham JM (2017) Experimental cyclic testing of URM pier-spandrel substructures. *J Struct Eng* 143(2):04016177. [https://doi.org/10.1061/\(ASCE\)ST.1943-541X.0001650](https://doi.org/10.1061/(ASCE)ST.1943-541X.0001650)
- Oats RC, Dai Q, Head M (2022) Digital image correlation advances in structural evaluation applications: a review. *Pract Period Struct Des Constr* 27(4):03122007. [https://doi.org/10.1061/\(ASCE\)SC.1943-5576.0000725](https://doi.org/10.1061/(ASCE)SC.1943-5576.0000725)
- Parisi F, Augenti N, Prota A (2014) Implications of the spandrel type on the lateral behavior of unreinforced masonry walls. *Earthq Engng Struct Dyn* 43:1867–1887. <https://doi.org/10.1002/eqe.2441>
- Rinaldin G, Amadio C, Gattesco N (2017) Review of experimental cyclic tests on unreinforced and strengthened masonry spandrels and numerical modelling of their cyclic behaviour. *Eng Struct* 132:609–623. <https://doi.org/10.1016/j.engstruct.2016.11.063>
- Tomažević M (1999) Earthquake-resistant design of masonry buildings. Series on innovation in structures and construction. Imperial College Press, London. <https://doi.org/10.1142/p055>

Publisher's Note Springer Nature remains neutral with regard to jurisdictional claims in published maps and institutional affiliations.